communications physics

Article

https://doi.org/10.1038/s42005-024-01630-9

Static vector solitons in a topological mechanical lattice

Check for updates

Yuan Zhou [1], Yafei Zhang [2], Jiaxin Long[1], Aoxi Wang[1] & Chang Qing Chen [1]

Topological solitons, renowned for their stability and particle-like collision behaviors, have sparked interest in developing macroscopic-scale information processing devices. However, the exploration of interactions between multiple topological solitons in mechanical systems remains elusive. In this study, we construct a topological mechanical lattice supporting static vector solitons that represent quantized degrees of freedom and can freely propagate across the system. Drawing inspiration from coupled double atomic chains with sublattice symmetry breaking, we design a mechanical analogue featuring topologically protected boundary modes and induce independent modes to finite motions along branched motion pathways. Through a continuum theory, we describe the evolution of boundary modes with vector solitons composed of superposed kink solutions, identifying them as minimum energy pathways on the rugged effective potential surface with multiple degenerate ground states. Our results reveal the connection between transformable topological lattices and multistable systems, providing insight into nonlinear topological mechanics.

Topological solitons, such as kinks, vortices, and skyrmions, have been extensively investigated to unveil underlying mechanisms in various systems, including conducting polymers[1], dislocation slipping[2], magnetic domain walls[3], DNA mobility[4], and light modulation in liquid crystals[5], among others[6]. These nontrivial excitations not only maintain stable profiles due to their non-perturbative topological robustness[7,8] but also exhibit particle-like collision behaviors[9]. Interactions involving multiple solitons have garnered increasing attention, revealing anomalous properties such as annihilation[10,11], and chiral switching[12]. These robust information carriers hold promise for topologically protected information processing and have the potential for applications in designing memory and logic devices[13,14].

In recent years, there has been a surge of interest in the exploration of kinks, topological solitons involved with a scalar field[6], within macroscopic mechanical metamaterials[15]. Researchers are actively employing engineered structural motifs to elucidate fundamental nonlinear phenomena and advance functional applications[16]. Typical examples include programmable localized deformations[17–20], robust transition fronts in elastic metamaterials[21,22], and topological mechanical lattices[23–25]. These transition fronts serve as mechanical signals and can be harnessed to design mechanical logic[26,27] and actuate soft robots[28]. However, most mechanical systems only support a single soliton, and the observation of interactions between multiple solitons has remained elusive[29,30].

Investigations into topological Maxwell lattices provide an avenue to nontrivial excitations[31–33]. Topological lattices are a special class of frames on the verge of instability characterized by a balanced number of degrees of freedom (DoFs) and constraints[34]. In one-dimensional topological lattices analogous to the Su-Schrieffer-Heeger (SSH) model for polyacetylene, a Peierls distorted chain with two ground-state configurations connected by a unique kink[1,35], both boundary mode and conductive soliton have been revealed[36,37]. Recent studies on atomic chains have introduced coupled double chains of indium atomic wires with sublattice symmetry breaking and chiral solitons, which are protected by a nontrivial configuration space with multiple ground states[7,38]. However, the long-range interactions of atomic chains hinder the manifestation of intriguing soliton behaviors in topological mechanical lattices.

In this paper, we report static vector solitons in a topological mechanical lattice, illustrating the interaction of dual DoFs. Specifically, we design a topological mechanical lattice with four-fold degenerate ground states and identify independent boundary modes. These modes are finitely deformable and can propagate through the bulk in terms of different kinds of solitons. In contrast to traditional solitons described by ϕ^4 or sine-Gordon equations[6,39], the vector solitons here arise from coupled field equations[40] and feature components admitting the sum or difference of two kinks, as shown in Fig. 1. This intriguing characteristic is relatively rare in mechanical systems and has primarily been demonstrated in the context of ferroelectric phase transitions, nonlinear optics, and multispecies condensates[41–43]. A deeper understanding obtained through an effective potential energy density reveals the criterion for the existence of four degenerate ground

[1]Department of Engineering Mechanics, CNMM and AML, Tsinghua University, 100084 Beijing, China. [2]Racah Institute of Physics, The Hebrew University of Jerusalem, Jerusalem 91904, Israel. e-mail: chencq@tsinghua.edu.cn

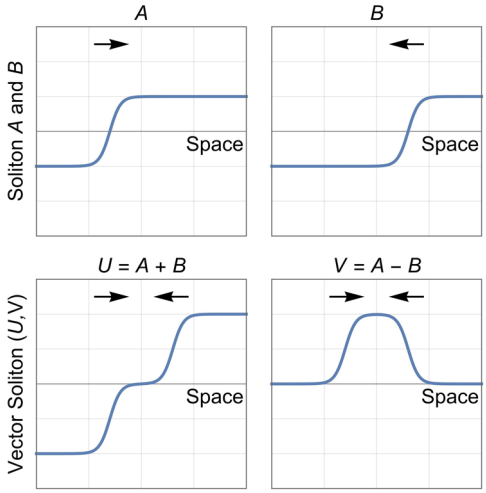

Fig. 1 | Vector solitons with superimposed components. Classic topological solitons (kinks A and B) are described by hyperbolic solutions, while vector solitons (U, V) derived from special coupled equations have components consisting of the sum and the difference of two sub-solitons.

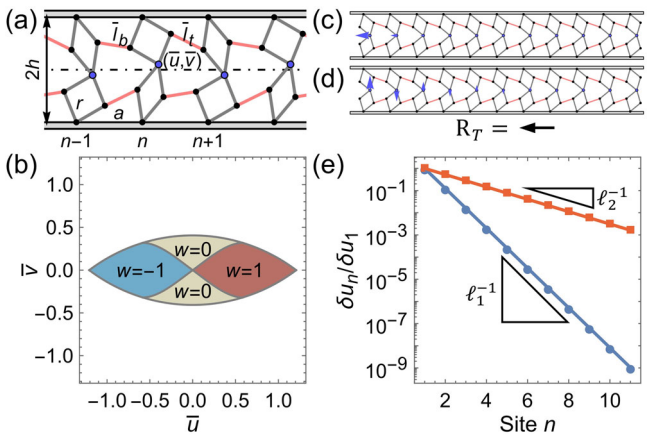

Fig. 2 | Topological mechanical lattices with polarized boundary states. a The mechanical lattice comprises gray hinged rhombic linkages, characterized by blue common nodes with translational degrees of freedom, interconnected by red bonds. The lattice's equilibrium configuration has nodal positions $(\bar{u}, \bar{v})$ and initial bond lengths $\bar{l}_b$ or $\bar{l}_t$. **b** The phase diagram of the lattice geometries $(\bar{u}, \bar{v})$ is divided into three topologically distinct phases based on the winding numbers defined in Eq. (1). **c**, **d** The equilibrium configuration $(\bar{u}, \bar{v}) = (u_s, 0)$ with free boundaries has two independent zero modes localized at the left end, denoted by blue arrows. The calculated topological polarization for the lattice is $\mathbf{R}_T = -\boldsymbol{a}$. **e** The polarized boundary modes decay exponentially into the bulk, characterized by two distinct penetration depths.

states in distorted lattices, and the vector soliton solutions act as minimum energy pathways that interpolate ground states. Our results shed light on the study of multiple solitons on a macroscopic scale.

Results and discussion

Topological mechanical lattice characterization

Drawing inspiration from the coupled double Peierls-dimerized atomic chain[7,12,38], celebrated for its sublattice symmetry breaking and chiral edge states, our system is comprised of interconnected bonds (red) and hinged rhombic linkages (gray) pivoted to the laboratory frame (Fig. 2a). The mechanical lattice has fixed rhombic side length r, vertical height $2h$, and lattice spacing a, showcasing glide-reflection symmetry. Each distorted hinged rhombic linkage has two net DoFs that we characterize with the coordinates of the common node (blue), (u_n, v_n), where n is the index of the unit cell. The interconnected bonds provide two length constraints between neighboring unit cells, i.e., $l_{b,n}(u_{n-1}, v_{n-1}, u_n, v_n)$ and $l_{t,n}(u_n, v_n, u_{n+1}, v_{n+1})$. The detailed geometric relations between the bond lengths and nodal coordinates are explained in Supplementary Note 1. The equilibrium position of nodes is denoted as $(\bar{u}, \bar{v})$, and the interconnected bonds have initial lengths of either $\bar{l}_b$ or $\bar{l}_t$. Due to the balanced numbers of length constraints and DoFs under periodic boundary conditions, the mechanical lattice is a Maxwell lattice[35,44,45]. The topological property of a periodic Maxwell lattice's phonon spectrum reflects the distribution of zero modes within a finite lattice, stemming from the release of DoFs at the lattice boundaries by cutting bonds[29] (see Supplementary Note 2).

To characterize the topological property of the Maxwell lattice, we consider its response to perturbations and determine the compatibility matrix. Assuming the common nodes possess lumped mass featuring the coordinated deformation of the rigid hinged rhombic linkages, we only need to consider the elastic deformation of interconnected bonds. The compatibility matrix, denoted as $\mathbf{C}$, establishes a mapping between the infinitesimal displacements of nodes $\delta\mathbf{u} = (\delta u_1, \delta v_1, \delta u_2, \delta v_2, \ldots)$ and the elongations of bonds $\delta\mathbf{l} = (\delta l_{t,1}, \delta l_{b,1}, \delta l_{t,2}, \delta l_{b,2}, \ldots)$ by employing the Taylor expansion of the bond lengths, $\delta\mathbf{l} = \mathbf{C}\delta\mathbf{u}$. To determine the distribution of eigenmodes, we consider the periodically tessellated unit cells along the horizontal axis and perform a Fourier transformation on the displacements. This results in the Fourier-transformed compatibility matrix $\mathbf{C}(k)$ as a function of wave number k, which is a square matrix due to the balanced number of nodes and bonds in a unit cell. The phonon spectrum can be calculated from the dynamic matrix $\mathbf{D}(k) = m^{-1}\mathbf{C}^{\dagger}(k)k_e\mathbf{C}(k)$, where m and k_e are diagonal matrix of masses and spring constants. In Supplementary Fig. 2, we show that highly symmetric unit cell $(\bar{u}, \bar{v}) = (0, 0)$ has bulk zero modes at $k = 0$, and distorted mechanical lattices exhibit a gapped spectrum. For a Maxwell lattice, this band gap converts bulk zero modes to modes of non-zero frequency and localizes the required zero modes at open boundaries[46]. Furthermore, the localization of boundary modes at specific ends can be characterized by the winding number of the phase of $\det \mathbf{C}(k)$, which separates topologically distinct bulk phases. Here, we adopt standard unit cell (see Supplementary Fig. 3) and the winding number is

$$w = \frac{1}{2\pi i}\int_{-\pi}^{\pi}\frac{d}{dk}\ln\det\mathbf{C}(k)dk. \tag{1}$$

The phase diagram of the lattices, depicted in Fig. 2b, reveals three distinct phases, each distinguished by their respective winding numbers. The admissible region for shaping linkages is constrained to $u^2 + (\bar{v} \pm h)^2 \le 4r^2$, as rhombic linkages cannot be connected outside of this region. Exploring the internal boundaries of the phase diagram, we determine the critical configurations through numerical calculations. These configurations do not appear to be associated with any obvious symmetry breaking, indicating a topological transition. The topological invariants can be used to define the topological polarization $\mathbf{R}_T = -w\boldsymbol{a}$, which transfer the DoFs along the polarization direction[35].

To illustrate the topological boundary modes, we consider mechanical lattices with open boundary conditions. In a finite lattice, there are two additional DoFs due to cutting interconnected bonds at the free boundaries. According to the Maxwell-Calladine index theorem[29,47], there exist two zero modes in the absence of states of self-stress. An example is showcased in Fig. 2c, d, where the equilibrium position of nodes is $(\bar{u}, \bar{v}) = (u_s, 0)$, and the topological polarization is $\mathbf{R}_T = -\boldsymbol{a}$. Two orthogonal zero modes, calculated from the null space of the finite lattice's compatibility matrix, localize at the left end, denoted by blue arrows. The horizontal and vertical zero modes decay exponentially into the bulk, characterized by inverse penetration depths $\ell_1^{-1} = \kappa_1$ and $\ell_2^{-1} = \kappa_2$ (Fig. 2e), where $i\kappa_1$ and $i\kappa_2$ constitute the complex wave numbers of the Fourier-transformed compatibility matrix, satisfying $\det\mathbf{C}(k = i\kappa) = 0$.

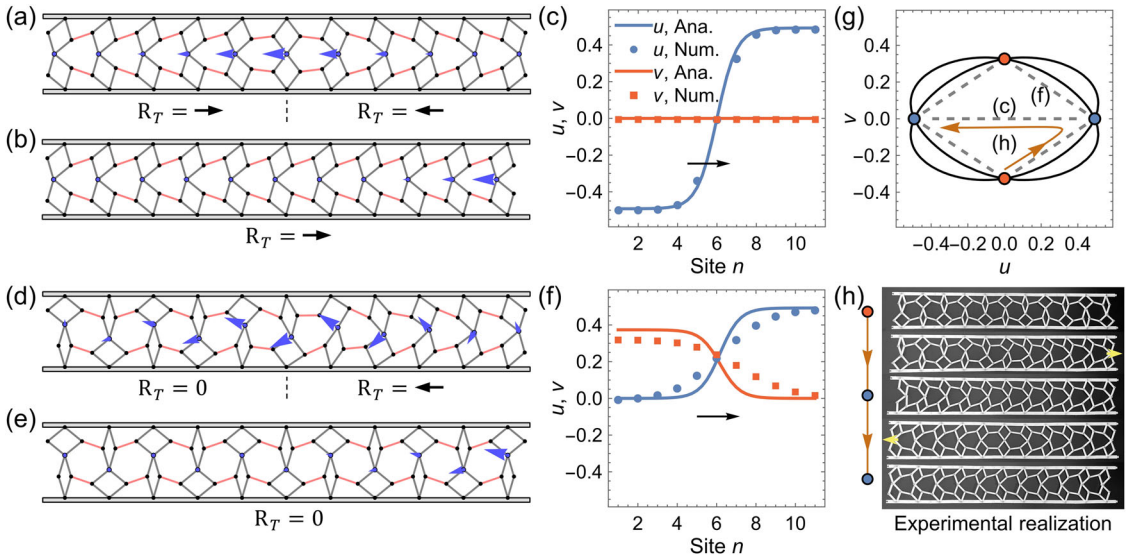

Fig. 3 | Nonlinear deformations and vector soliton excitations. a The transformed configuration exhibits a domain wall, interpolating two opposite topological states under an applied perturbation of horizontal zero mode. The center of the domain wall is denoted by a vertical dash line. **b** The lattice is transformed to $(-u_s, 0)$. **c** Iteratively generated coordinates of common nodes for the finite lattice (markers) align closely with the corresponding analytical prediction (lines). The horizontal components show a profile of kink, while the vertical components remain zero. The arrow indicates the domain wall propagation direction. **d** The transformed configuration exhibits a domain wall interpolating trivial and nontrivial topological states under an applied perturbation of vertical zero mode. **e** The lattice is transformed to $(0, v_s)$. **f** The horizontal and vertical components exhibit a profile of kink and antikink co-propagating across the lattice. **g** The four homogeneous configurations, sharing the same bond length, are derived from the zero-energy constraint equations. Domain walls connecting these configurations are represented by the gray dashed lines. **h** Experimental results of the prototype's evolution along the customized transition pathways (marked by the solid orange line with arrows) reveal multiple homogeneous configurations.

Multiple degenerate ground states

One-dimensional isostatic lattices are known to facilitate the propagation of conductive solitons through the system when polarized boundary modes are integrated to finite deformations[23–25,31–33]. In contrast, the topological mechanical lattice possesses independent horizontal and vertical boundary modes, along with branched motion pathways in its initial configuration. By exploring its nonlinear excitations corresponding to different zero modes, we expect to unveil exotic features beyond the realm of classic single solitons. In order to induce these intriguing nonlinear excitations, we conform the lattice along the two orthogonal modes, respectively. Specifically, we numerically calculate the evolution of the lattice from its initial state by gradually applying perturbations to the node situated at the polarized boundary (see Supplementary Note 3). The zero-energy constraint equations have the following forms, i.e.,

$$l_t^2(u_n, v_n, u_{n+1}, v_{n+1}) = \bar{l}_t^2, \tag{2}$$

$$l_b^2(u_n, v_n, u_{n+1}, v_{n+1}) = \bar{l}_b^2. \tag{3}$$

When the first node position is given, the constraints act as a map iteration to obtain the position of next node in the series, leading to a cascade of transformations.

First, the transformed configuration along the horizontal direction is presented in Fig. 3a. From the left end to the bulk until the right end (Fig. 3b), the nodes gradually translate from $(u_s, 0)$ to $(-u_s, 0)$. According to the phase diagram, the transformed region possesses a reversed winding number, corresponding to a flipped topological polarization. The domain wall that interpolates between the nontrival topological phases, displaying a classic kink profile for the horizontal component u_n, while the vertical component v_n remains zero (markers in Fig. 3c). The updated horizontal zero mode is depicted on the transformed configuration and it is always localized at the center of the domain wall. Nonetheless, the system with multiple topological phases can exhibit more intriguing behavior when a perturbation of vertical zero mode is applied to the homogeneous configuration.

The transformed configuration, illustrated along with the vertical pathway in Fig. 3d, demonstrates the simultaneous coexistence of both trivial and nontrivial topological phases. The domain wall connecting these phases freely propagates through the bulk, until all common nodes display alternating vertical offsets (Fig. 3e). In contrast to SSH chains with a single order parameter, the nodes approach $(0, v_s)$ from $(u_s, 0)$, and the two components demonstrate kink and antikink co-propagating across the lattice (Fig. 3f). As a consequence of the nonlinear deformations, the topological mechanical lattice shows four homogeneous configurations calculated from Eqs. (2) and (3), denoted as $(\pm u_s, 0)$ and $(0, \pm v_s)$ (blue and orange dots in Fig. 3g). These four homogeneous configurations have different topological indexes and are located in classified region in the phase diagram (see Supplementary Fig. 4). The domain wall initiating from one state to another corresponds to different pathways among them. To customize the transition pathways and illustrate the domain walls, we construct a physical prototype and experimentally validate the transformation from $(0, -v_s)$ to $(u_s, 0)$ to $(-u_s, 0)$ as shown in Fig. 3h. We progressively applied displacements to the end node of the lattice, observing the resulting deformed microstructures. Moreover, applying loads to different edges reveals significant differences in edge stiffness, a characteristic commonly associated with polarized lattices[48,49] (see Supplementary Note 4).

Superposed sub-solitons

To uncover the underlying physics of the nonlinear response, we derive a continuum model and seek analytical soliton solutions. The lattice spacing a is assumed to be much smaller than the varying components u_n and v_n, allowing us to define the field variables $u(x)$ and $v(x)$ at the long wave limit, where $x = n + 1/2$. With this approximation, the node coordinates can be represented as the field variables and their derivatives. Consequently, Eqs. (2) and (3) become ordinary differential equations, which are elaborated in Supplementary Note 5A. By employing Taylor series expansions up to the second order for the field variables and first order for the derivatives, respectively, the zero-energy constraint equations are further simplified as

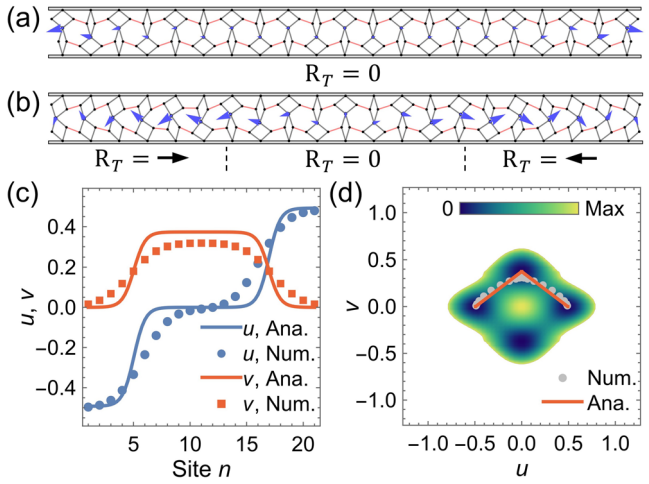

Fig. 4 | Multiple degenerate ground states and domain structure. a The trivial configuration with zero mode denoted by blue arrows. **b** The domain structure separates the trivial regions and different polarized phases, denoted as polarization vectors $\mathbf{R}_T$. **c** The distributions of horizontal and vertical nodal positions, calculated from the map iteration (u and v, markers). The vector soliton solutions (lines) within the domain structure exhibit linear combinations of two kink solutions. **d** The trajectory of the vector soliton is shown in the projection of the effective potential energy density, smoothly interpolating the three ground states. The color bar represents the value of effective potential energy density.

follows

$$\alpha\left[(U+V)^2-\left(\bar{U}+\bar{V}\right)^2\right]+U'+V'=0, \tag{4}$$

$$\alpha\left[(U-V)^2-\left(\bar{U}-\bar{V}\right)^2\right]+U'-V'=0. \tag{5}$$

with the normalized coordinates

$$\begin{aligned} U&=\tfrac{a-u_m}{r^2}u,\ V=\tfrac{h(a-u_m)}{u_m r^2}v,\\ \bar{U}&=\tfrac{a-u_m}{r^2}\bar{u},\ \bar{V}=\tfrac{h(a-u_m)}{u_m r^2}\bar{v}, \end{aligned} \tag{6}$$

where $\alpha=r^2\left(4ar^2-u_m h^2\right)/\left[u_m h^2\left(a-u_m\right)^2\right]$ is the normalized coefficient and $u_m=\left(4r^2-h^2\right)^{1/2}$ is the upper bound of the horizontal component.

These coupled equations commonly arise in the fields of multiferroic phase transitions, nonlinear optics and multispecies condensates[40–43], supporting vector soliton solutions. We solve the equations using variables $U+V$ and $U-V$, leading to nontrivial solutions in addition to the trivial ones, $(U,V)=\pm\left(\bar{U},\bar{V}\right)$ and $(U,V)=\pm\left(\bar{V},\bar{U}\right)$. The system allows for superposed kink solutions

$$\begin{aligned} U(x)\ =\ &\frac{\bar{U}+\bar{V}}{2}\tanh[\alpha(\bar{U}+\bar{V})(x-x_l)]\\ &+\frac{\bar{U}-\bar{V}}{2}\tanh[\alpha(\bar{U}-\bar{V})(x-x_r)] \end{aligned} \tag{7}$$

$$\begin{aligned} V(x)\ =\ &\frac{\bar{U}+\bar{V}}{2}\tanh[\alpha(\bar{U}+\bar{V})(x-x_l)]\\ &-\frac{\bar{U}-\bar{V}}{2}\tanh[\alpha(\bar{U}-\bar{V})(x-x_r)] \end{aligned} \tag{8}$$

where x_l and x_r are integration constants representing the centers of sub-solitons. The vector soliton shows superposed hyperbolic solutions, a unique phenomenon in soliton physics, and can be used to account for soliton collisions[40]. Note that the constants in the equations determine the number of independent DoFs in the finite lattice and govern the position and profile of the superposed solutions. For the initial configuration $(\bar{u},\bar{v})=\left(u_s,0\right)$, when $x_l=x_r$, it indicates that the positions of the two sub-solitons coincide, resulting in the superposed solution reducing to the solution with a single nontrivial component $U(x)=\bar{U}_s\tanh\left[\alpha\bar{U}_s\left(x-x_l\right)\right]$ and $V(x)=0$, which resembles the kink in SSH chains. As shown in Fig. 3c, the obtained kink solution agrees well with the numerical results. The insightful solution with co-propagating domain walls in Fig. 3f indicates that $x_l\to-\infty$ and x_r represents the center of the kink and antikink. These results reveal the capability of the topological mechanical lattice to support static vector solitons with components. The term 'vector solitons' has been previously used in the context of Korteweg–de Vries(KdV)-like solitons of monostable elastic metamaterials with coupled translational-rotational components[50–52], arising from a subtle balance between nonlinear and dispersion effects. However, the vector solitons presented in topological mechanical lattices stem from multiple degenerate ground states, exhibiting substantial differences from the elastic pulse[39]. These vector solitons feature the microstructural evolution of zero-energy configurations and can be triggered with minimal energy input, unlike elastic pulses with amplitude gaps. Polarized zero modes and solitons in topological lattices can even be actuated in an active bath with thermal fluctuations[53]. Furthermore, the system allows for the superposition of sub-solitons, which is rare in mechanical systems.

To gain deeper insight into the configuration space, we derive an effective potential energy density $P(u,v)$ for the lattice (see Supplementary Note 5B)

$$\begin{aligned} P\ =\ &\frac{k_e r^4}{8\bar{l}_t^{\,2}}\alpha^2\left[(U+V)^2-(\bar{U}+\bar{V})^2\right]^2\\ &+\frac{k_e r^4}{8\bar{l}_b^{\,2}}\alpha^2\left[(U-V)^2-(\bar{U}-\bar{V})^2\right]^2. \end{aligned} \tag{9}$$

The nonlinear deformations in our system carry clear physical significance. The trivial solutions correspond to the four distinct ground states, while the soliton solutions represent the transition states on the effective energy surface. This behavior is an analog to the double Perierls chain model, where the dimerization displacements of each chain lead to symmetry breaking of the total energy surface, and chiral solitons are excited at domain boundaries between ground states[7,12]. In our case, the vector solitons switch distinct topological phases and transfer zero modes from the boundary into the bulk. The sub-solitons represent quantized DoFs, displaying particle-like collision behaviors during their propagation. The total energy is maintained at zero due to a balance between the energy barrier arising from the effective potential and the contributions from other gradient and integrable terms. These remarkable properties further highlight the topologically transformable nature of our system.

The independent integration constants x_l and x_r in Eqs. (7) and (8) enable the sub-solitons to either approach or depart from each other. This feature demonstrates that the topological mechanical lattice can be used to generate multiple topological phases. A schematic of the transformed configuration $(0,v_s)$ is presented in Fig. 4a, representing a topologically trivial state with boundary modes on each open edge. The evolution of the domain structure along linearly superposed modes is illustrated in Fig. 4b, where the trivial phase is separated by opposite topological polarized phases. We demonstrate the domain wall profiles by numerical iterations of (2) and (3) and analytical solutions of (7) and (8). Both results show three phases separated by two domain walls (Fig. 4c), which further reflects the linear combinations of two kink solutions. The coexistence of three phases resembles the stationary domain wall in rotating-squares structure with embedded magnets, which demonstrates a tristable energy landscape[54]. Further analysis highlights a general view, i.e., different phases can be interpolated by the minimum energy pathway in multistable systems.

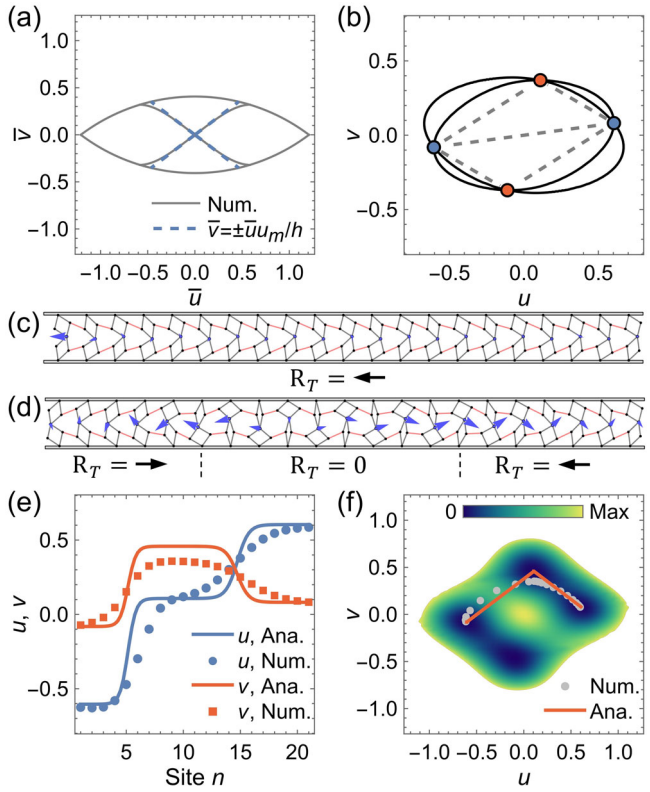

Fig. 5 | Vector solitons in general lattices. a The boundary lines of critical configurations at the topological transitions in the phase diagram. **b** Four homogeneous configurations (dots) with the same bond length are determined from the zero-energy constraint equations of lattice $(\bar{u},\bar{v}) = (1.23u_s, 0.25v_s)$, and the domain walls (lines) connect different phases. **c** Schematic of the polarized lattice, with polarization vector $\mathbf{R}_T$ oriented towards left free boundary. **d** The distorted region in the domain structure features the trivial phase separated by opposite topological phases. **e** The distributions of nodal positions (u and v, markers) and vector solitons (lines) within the domain structure exhibit linear combinations of two kinks with different amplitudes. **f** The effective potential energy density exhibits four degenerate ground states. The vector soliton corresponds to the minimum energy pathway on the rugged energy surface. The color bar denotes the value of effective potential energy density.

Figure 4d shows the trajectory of the vector soliton on the surface of effective potential energy density, projecting the minimum energy pathway on the rugged energy surface. This trajectory highlights how the vector soliton smoothly interpolates these phases.

General lattices

By virtue of the continuum model, we can extend the concept of multiple degenerate configurations and vector soliton solutions to any state. The critical states at topological transition in the phase diagram can be determined when the four degenerate ground states degrade into double ground states: $|\bar{U}| = |\bar{V}|$. According to the Eq. (6), we derive the boundary lines $\bar{v} = \pm\bar{u}u_m/h$ as blue dashed lines shown in Fig. 5a, which slightly deviate for large $(|\bar{u}|, |\bar{v}|)$ due to the second-order approximation in the theoretical model (Eqs. (4) and (5)). The analytical predictions offer a convenient method for identifying polarization changes based on geometric parameters, without the need to calculate phonon bands. Furthermore, we investigate the criterion for the existence of multiple ground states (see Supplementary Note 5C). For any given lattice within the predicted admissible region, there will always be four homogeneous configurations with the same bond length, each located in distinct regions of the phase diagram representing different topological phases.

As an example, we demonstrate a distorted lattice $(\bar{u},\bar{v}) = (1.23u_s, 0.25v_s)$ and calculate the homogeneous configurations using the cross-points of Eqs. (2) and (3) as shown in Fig. 5b. It exhibits a topological polarization of $\mathbf{R}_T = -\boldsymbol{a}$, with two boundary modes localized at the left end (Fig. 5c). The corresponding domain structure with multiple topological phases is illustrated in Fig. 5d, where the trivial phase is separated by opposite topological polarized phases. Evolution of the lattice along its conformational motions leads to the formation of sub-solitons with different amplitudes and their linear combinations remain effective (Fig. 5e). Despite the effective potential energy density for lattices $(u_s, 0)$ or $(0, v_s)$ mentioned above exhibits high symmetries, the surface for the general lattice retains inversion symmetry $P(u, v) = P(-u, -v)$. Hence, the distorted lattice can also support domain structures with multiple topological phases. The trajectory for the hybrid structure, projected onto the energy surface, is shown in Fig. 5f. The vector soliton (line) quantitatively captures the numerical results (markers), interpolating between multiple ground states. These general cases demonstrate the vector solitons exist widely in the class of topological mechanical lattices. Moreover, although our emphasis is on the static character of vector solitons, dynamic responses also showcase the superposition of sub-solitons when subjected to a boost (see Supplementary Note 5D).

Conclusions

We have demonstrated a class of vector solitons within transformable topological mechanical lattices, inspired by the coupled double atomic chains. The introduced DoFs in the finite isostatic lattice manifest as independent boundary modes and propagating sub-solitons capable of switching initial configurations. The vector solitons, composed of superposed hyperbolic solutions, demonstrate reversible microstructure evolution and the capability to reverse topological polarizations. Our work inspires the development of additional models for macroscopic lattices that are analogous to crystal structures, involving fixed boundaries and connected rotating blocks. This conceptual framework has potential applications in exploring other topological properties experimentally[55–57]. Additionally, our study reveals the connection between topological lattices and multistable systems, presenting challenges for describing transformable topological systems through geometric insights[33,58]. Finally, the observed multiple soliton interactions indicate the possibility of developing functional devices, such as soliton-based logic gates[59], diodes[60], and algebraic operations in mechanical computing systems.

Methods

Compatibility matrix and phonon spectrum

Using the geometric relationships of connecting bonds between neighboring unit cells, i.e., $l_{b,n}(u_{n-1}, v_{n-1}, u_n, v_n)$ and $l_{t,n}(u_n, v_n, u_{n+1}, v_{n+1})$, we can compute the compatibility matrix by expanding the bond lengths through Taylor series

$$\begin{pmatrix} \delta l_{b,n} \\ \delta l_{t,n} \end{pmatrix} = \begin{pmatrix} c_{00} & d_{00} & c_{01} & d_{01} & 0 & 0 \\ 0 & 0 & c_{10} & d_{10} & c_{11} & d_{11} \end{pmatrix} \begin{pmatrix} \delta u_{n-1} \\ \delta v_{n-1} \\ \delta u_n \\ \delta v_n \\ \delta u_{n+1} \\ \delta v_{n+1} \end{pmatrix}, \quad (10)$$

where c_{ij} are the linearized coefficients.

In periodic lattices, the nodal displacements corresponding to a phonon mode exhibit a Bloch form, given as $(\delta u_n, \delta v_n) = (\delta\tilde{u}, \delta\tilde{v})e^{ikn}e^{-i\omega t}$, where $\delta\tilde{u}$ and $\delta\tilde{v}$ denote infinitesimal displacements within a reference unit cell. When we substitute the Bloch solution into the compatibility equation, we derive a transformed compatibility matrix. This matrix is square due to the same number of nodes and bonds in a unit cell.

$$\mathbf{C}(k) = \begin{pmatrix} c_{00}e^{-ik} + c_{01} & d_{00}e^{-ik} + d_{01} \\ c_{10} + c_{11}e^{ik} & d_{10} + d_{11}e^{ik} \end{pmatrix} \quad (11)$$

According to the equation of motion, the eigenfrequencies of the lattice are determined by $\left|m^{-1}\mathbf{C}^{T}k_{e}\mathbf{C}-\omega^{2}\mathbf{I}\right|=0$, where $\mathbf{I}$ is the identity matrix. The phonon spectrum, as a function of wave numbers k, can be derived from the dynamic matrix $\mathbf{D}(k)=m^{-1}\mathbf{C}^{\dagger}(k)k_{e}\mathbf{C}(k)$. It's common to set the spring constants and masses to unity for simplicity. A gapped spectrum implies the absence of bulk zero modes but the presence of boundary modes, and the phonon band can be featured by the winding number Eq. (1).

Map iteration and numerical simulation

To quantitatively characterize the nonlinear deformations in the isostatic lattice, we use the zero-energy constraints defined by constant bond lengths Eqs. (2) and (3). These constraints form a map iteration denoted by $\left(u_{n+1},v_{n+1}\right)=f\left(u_{n},v_{n}\right)$, where, the shape of the initial unit is given, the coordinates of neighboring sites are determined and serve as inputs for the subsequent sites[31]. The nodal displacement of the initial unit is given based on their boundary modes, and these coupled equations are solved using Newton's method. By repeatedly applying the map iteration $\left(u_{n+1},v_{n+1}\right)=f^{n}\left(u_{1},v_{1}\right)$, we identify the fixed points of this iterative process, denoted as $(u^{*},v^{*})=f(u^{*},v^{*})$. The fixed points correspond to homogeneous configurations and the mechanical lattice in Fig. 3 has four fixed points $\left(\pm u_{s},0\right)$ and $\left(0,\pm v_{s}\right)$, reflecting multiple ground states. As the initial unit evolves along the horizontal or vertical zero mode, the units are successively transformed towards the right boundary, leading to distinct homogeneous configurations in the system as shown in Fig. 3a, d. At each step of the transformation, the zero modes are directly calculated from the compatibility matrix using the nodal positions of current configuration.

Physical prototype and polarized boundary stiffness

To demonstrate the transformation process, a physical prototype with fixed geometric parameters $(r,h,a)=(20\,\mathrm{mm},31.8\,\mathrm{mm},40\,\mathrm{mm})$ has been created utilizing printed linkages (photosensitive resin DSM IMAGE8000) and metal screws, as depicted in Fig. 3h. The hard components and isostaticity within the bulk ensure that by controlling the nodal position at the lattice boundary, the configuration remains well-determined. The lattice $(\bar{u},\bar{v})=\left(u_{s},0\right)$ exhibits four homogeneous configurations, which are located in the classified regions in the phase diagram and can be transformed among each other. In Fig. 3g, we customize the transition pathway as indicated by the curved arrow. Starting from the initial state $\left(0,-v_{s}\right)$, we apply displacements on the right boundary, directed outward as the yellow arrow shown in the Fig. 3h. This introduces a domain wall from the right to the left end, leading to the transformation of the lattice to $\left(u_{s},0\right)$. Subsequently, a similar procedure is duplicated except the displacements are applied from the left end. The lattice is finally transformed to configuration $\left(-u_{s},0\right)$. Considering the inherent limitations related to assembly precision and component friction, it is found that applying horizontal displacements is more effective in deforming the lattice, although these pathways are reversible.

To demonstrate the dramatic differences in edge stiffness, measured as the ratio of force to displacement, in the lattice $\left(u_{s},0\right)$, we maintain the laboratory frame fixed to the ground and apply 2 mm displacements at both edges. The results demonstrate a drag force of 0.05 N at the soft edge and 8.80 N at hard edge, as shown in Fig. S4c, d, revealing a significant two-order magnitude difference in stiffness contrast due to the topological polarization.

Criterion for the existence of vector soliton

To identify the admission region with multiple ground states, we examine the transformed states as predicted by the theoretical model. Our analytical vector soliton solutions do not impose additional geometric requirements. For a general lattice with extreme distortion, the transformed states can be expressed as $\bar{u}'=\bar{v}h/u_{m}$ or $\bar{v}'=\bar{u}u_{m}/h$ according to Eq. (6). The transformation introduces an extra constraint described by the inequality

$$\left(\frac{\bar{v}h}{u_{m}}\right)^{2}+\left(\frac{\bar{u}u_{m}}{h}\pm h\right)^{2}\leq 4r^{2}. \tag{12}$$

The area of overlap between this transformed region and the initial admissible region defines the region where vector solitons can exist, as illustrated in Supplementary Fig. S6b. An extreme case is presented in Supplementary Fig. S6c, and larger geometric parameters raise concerns about connectivity in these lattices.

Data availability

The data that support the findings of this study can be provided from the corresponding author upon reasonable request.

Code availability

The code used for the analysis is available from the authors upon reasonable request.

Received: 26 December 2023; Accepted: 15 April 2024;
Published online: 22 April 2024

References

1. Su, W. P., Schrieffer, J. R. & Heeger, A. J. Solitons in polyacetylene. *Phys. Rev. Lett.* **42**, 1698–1701 (1979).
2. Braun, O. M. & Kivshar, Y. S. Nonlinear dynamics of the Frenkel–Kontorova model. *Phys. Rep.* **306**, 1–108 (1998).
3. Braun, H.-B. et al. Emergence of soliton chirality in a quantum antiferromagnet. *Nat. Phys.* **1**, 159–163 (2005).
4. Yakushevich, L. V., Savin, A. V. & Manevitch, L. I. Nonlinear dynamics of topological solitons in DNA. *Phys. Rev. E* **66**, 016614 (2002).
5. Hess, A. J., Poy, G., Tai, J.-S. B., Žumer, S. & Smalyukh, I. I. Control of light by topological solitons in soft chiral birefringent media. *Phys. Rev. X* **10**, 031042 (2020).
6. Manton, N. & Sutcliffe, P. *Topological Solitons*. (Cambridge University Press, 2004).
7. Cheon, S., Kim, T.-H., Lee, S.-H. & Yeom, H. W. Chiral solitons in a coupled double Peierls chain. *Science* **350**, 182–185 (2015).
8. Im, T., Song, S. K., Park, J. W. & Yeom, H. W. Topological soliton molecule in quasi 1D charge density wave. *Nat. Commun.* **14**, 5085 (2023).
9. Ackerman, P. J. & Smalyukh, I. I. Static three-dimensional topological solitons in fluid chiral ferromagnets and colloids. *Nat. Mater.* **16**, 426–432 (2017).
10. Petrović, M. D., Bajpai, U., Plecháč, P. & Nikolić, B. K. Annihilation of topological solitons in magnetism with spin-wave burst finale: Role of nonequilibrium electrons causing nonlocal damping and spin pumping over ultrabroadband frequency range. *Phys. Rev. B* **104**, L020407 (2021).
11. Park, J. W. et al. Creation and annihilation of mobile fractional solitons in atomic chains. *Nat. Nanotechnol.* **17**, 244–249 (2022).
12. Kim, T.-H., Cheon, S. & Yeom, H. W. Switching chiral solitons for algebraic operation of topological quaternary digits. *Nat. Phys.* **13**, 444–447 (2017).
13. Allwood, D. A. et al. Magnetic domain-wall logic. *Science* **309**, 1688–1692 (2005).
14. Fert, A., Reyren, N. & Cros, V. Magnetic skyrmions: advances in physics and potential applications. *Nat. Rev. Mater.* **2**, 17031 (2017).
15. Deng, B., Raney, J. R., Bertoldi, K. & Tournat, V. Nonlinear waves in flexible mechanical metamaterials. *J. Appl. Phys.* **130**, 040901 (2021).
16. Bertoldi, K., Vitelli, V., Christensen, J. & van Hecke, M. Flexible mechanical metamaterials. *Nat. Rev. Mater.* **2**, 17066 (2017).
17. Machon, T., Alexander, G. P., Goldstein, R. E. & Pesci, A. I. Instabilities and solitons in minimal strips. *Phys. Rev. Lett.* **117**, 017801 (2016).
18. Zhang, Y., Li, B., Zheng, Q. S., Genin, G. M. & Chen, C. Q. Programmable and robust static topological solitons in mechanical metamaterials. *Nat. Commun.* **10**, 5605 (2019).

19. Deng, B., Yu, S., Forte, A. E., Tournat, V. & Bertoldi, K. Characterization, stability, and application of domain walls in flexible mechanical metamaterials. *Proc. Natl. Acad. Sci.* **117**, 31002–31009 (2020).
20. Sun, K. & Mao, X. Fractional excitations in non-Euclidean elastic plates. *Phys. Rev. Lett.* **127**, 098001 (2021).
21. Kochmann, D. M. & Bertoldi, K. Exploiting microstructural instabilities in solids and structures: from metamaterials to structural transitions. *Appl. Mech. Rev*. **69**, 050801 (2017).
22. Jin, L. et al. Guided transition waves in multistable mechanical metamaterials. *Proc. Natl. Acad. Sci. USA* **117**, 2319–2325 (2020).
23. Chen, B. G., Upadhyaya, N. & Vitelli, V. Nonlinear conduction via solitons in a topological mechanical insulator. *Proc. Natl. Acad. Sci.* **111**, 13004–13009 (2014).
24. Zhou, Y., Chen, B. G., Upadhyaya, N. & Vitelli, V. Kink-antikink asymmetry and impurity interactions in topological mechanical chains. *Phys. Rev. E* **95**, 022202 (2017).
25. Sato, K. & Tanaka, R. Solitons in one-dimensional mechanical linkage. *Phys. Rev. E* **98**, 013001 (2018).
26. Raney, J. R. et al. Stable propagation of mechanical signals in soft media using stored elastic energy. *Proc. Natl. Acad. Sci.* **113**, 9722–9727 (2016).
27. Pal, A. & Sitti, M. Programmable mechanical devices through magnetically tunable bistable elements. *Proc. Natl. Acad. Sci.* **120**, e2212489120 (2023).
28. Deng, B., Zanaty, M., Forte, A. E. & Bertoldi, K. Topological solitons make metamaterials crawl. *Phys. Rev. Appl.* **17**, 014004 (2022).
29. Lubensky, T. C., Kane, C. L., Mao, X., Souslov, A. & Sun, K. Phonons and elasticity in critically coordinated lattices. *Rep. Prog. Phys.* **78**, 073901 (2015).
30. Xiu, H. et al. Synthetically non-Hermitian nonlinear wave-like behavior in a topological mechanical metamaterial. *Proc. Natl. Acad. Sci.* **120**, e2217928120 (2023).
31. Zhou, Y., Zhang, Y. & Chen, C. Q. Amplitude-dependent boundary modes in topological mechanical lattices. *J. Mech. Phys. Solids* **153**, 104482 (2021).
32. Kim, J. Z., Lu, Z., Blevins, A. S. & Bassett, D. S. Nonlinear dynamics and chaos in conformational changes of mechanical metamaterials. *Phys. Rev. X* **12**, 011042 (2022).
33. Ma, F. et al. Nonlinear topological mechanics in elliptically geared isostatic metamaterials. *Phys. Rev. Lett.* **131**, 046101 (2023).
34. Mao, X. & Lubensky, T. C. Maxwell lattices and topological mechanics. *Annu. Rev. Condens. Matter Phys.* **9**, 413–433 (2018).
35. Kane, C. L. & Lubensky, T. C. Topological boundary modes in isostatic lattices. *Nat. Phys.* **10**, 39–45 (2014).
36. Rajabpoor Alisepahi, A., Sarkar, S., Sun, K. & Ma, J. Breakdown of conventional winding number calculation in one-dimensional lattices with interactions beyond nearest neighbors. *Commun. Phys.* **6**, 334 (2023).
37. Upadhyaya, N., Chen, B. G. & Vitelli, V. Nuts and bolts of supersymmetry. *Phys. Rev. Res.* **2**, 043098 (2020).
38. Kim, T.-H. & Yeom, H. W. Topological solitons versus nonsolitonic phase defects in a quasi-one-dimensional charge-density wave. *Phys. Rev. Lett.* **109**, 246802 (2012).
39. Dauxois, T. & Peyrard, M. *Physics of Solitons*. (Cambridge University Press, 2006).
40. Khare, A. & Saxena, A. Superposed hyperbolic kink and pulse solutions of coupled $\phi 4$, NLS and mKdV equations. *Int. J. Mod. Phys. B* **36**, 2250142 (2022).
41. Ishibashi, Y. & Dvorák, V. Domain walls in improper ferroelectrics. *J. Phys. Soc. Jpn.* **41**, 1650–1658 (1976).
42. Rajaraman, R. Solitons of coupled scalar field theories in two dimensions. *Phys. Rev. Lett.* **42**, 200–204 (1979).
43. Cardoso, W. B., Avelar, A. T. & Bazeia, D. Modulation of localized solutions in a system of two coupled nonlinear Schrödinger equations. *Phys. Rev. E* **86**, 027601 (2012).
44. Meeussen, A. S., Paulose, J. & Vitelli, V. Geared topological metamaterials with tunable mechanical stability. *Phys. Rev. X* **6**, 041029 (2016).
45. Zhou, D., Zhang, L. & Mao, X. Topological boundary floppy modes in quasicrystals. *Phys. Rev. X* **9**, 021054 (2019).
46. Sun, K., Souslov, A., Mao, X. & Lubensky, T. C. Surface phonons, elastic response, and conformal invariance in twisted kagome lattices. *Proc. Natl. Acad. Sci.* **109**, 12369–12374 (2012).
47. Calladine, C. R. Buckminster Fuller's "Tensegrity" structures and Clerk Maxwell's rules for the construction of stiff frames. *Int. J. Solids Struct.* **14**, 161–172 (1978).
48. Bilal, O. R., Süsstrunk, R., Daraio, C. & Huber, S. D. Intrinsically polar elastic metamaterials. *Adv. Mater.* **29**, 1700540 (2017).
49. Xia, R., Nassar, H., Chen, H., Li, Z. & Huang, G. Microtwist homogenization of three-dimensional Pyrochlore lattices on zero modes and mechanical polarization. *J. Mech. Phys. Solids* **155**, 104564 (2021).
50. Deng, B., Raney, J. R., Tournat, V. & Bertoldi, K. Elastic vector solitons in soft architected materials. *Phys. Rev. Lett.* **118**, 204102 (2017).
51. Deng, B., Wang, P., He, Q., Tournat, V. & Bertoldi, K. Metamaterials with amplitude gaps for elastic solitons. *Nat. Commun.* **9**, 3410 (2018).
52. Deng, B., Tournat, V., Wang, P. & Bertoldi, K. Anomalous collisions of elastic vector solitons in mechanical metamaterials. *Phys. Rev. Lett.* **122**, 044101 (2019).
53. Woodhouse, F. G., Ronellenfitsch, H. & Dunkel, J. Autonomous actuation of zero modes in mechanical networks far from equilibrium. *Phys. Rev. Lett.* **121**, 178001 (2018).
54. Yasuda, H., Korpas, L. M. & Raney, J. R. Transition waves and formation of domain walls in multistable mechanical metamaterials. *Phys. Rev. Appl.* **13**, 054067 (2020).
55. Wu, Y., Chaunsali, R., Yasuda, H., Yu, K. & Yang, J. Dial-in Topological Metamaterials Based on Bistable Stewart Platform. *Sci. Rep.* **8**, 112 (2018).
56. Wang, A., Zhou, Y. & Chen, C. Q. Topological mechanics beyond wave dynamics. *J. Mech. Phys. Solids* **173**, 105197 (2023).
57. Wang, A., Meng, Z. & Chen, C. Q. Non-Hermitian topology in static mechanical metamaterials. *Sci. Adv.* **9**, eadf7299 (2023).
58. Rocklin, D. Z., Zhou, S., Sun, K. & Mao, X. Transformable topological mechanical metamaterials. *Nat. Commun.* **8**, 14201 (2017).
59. Chen, T., Bilal, O. R., Shea, K. & Daraio, C. Harnessing bistability for directional propulsion of soft, untethered robots. *Proc. Natl. Acad. Sci.* **115**, 5698–5702 (2018).
60. Zhou, D., Ma, J., Sun, K., Gonella, S. & Mao, X. Switchable phonon diodes using nonlinear topological Maxwell lattices. *Phys. Rev. B* **101**, 104106 (2020).

Acknowledgements

We would like to thank Prof. Bo Li for useful discussion. This work is supported by the National Natural Science Foundation of China (Nos. 12132007 and 11921002).

Author contributions

Y. Zhou and C.Q. Chen designed the research. Y. Zhou and Y. Zhang conducted numerical simulations. Y. Zhou, J. Long and A. Wang contributed to experimental characterization and theoretical analysis. C.Q. Chen supervised the project. All authors contributed to discussions and writing the manuscript.

Competing interests

The authors declare no competing interests.

Additional information

Supplementary information The online version contains supplementary material available at https://doi.org/10.1038/s42005-024-01630-9.

Correspondence and requests for materials should be addressed to Chang Qing Chen.

Peer review information *Communications Physics* thanks Wenting Cheng and the other, anonymous, reviewer(s) for their contribution to the peer review of this work. A peer review file is available.